Interseismic deformation from Sentinel-1 burst-overlap interferometry: Application to the southern Dead Sea fault

Xing Li[1], Sigurjón Jónsson[1], Yunmeng Cao[1]

[1]King Abdullah University of Science and Technology (KAUST), Thuwal, Saudi Arabia.

Corresponding author: Sigurjón Jónsson (sigurjon.jonsson@kaust.edu.sa)

Key Points:

- Along-track Sentinel-1 burst-overlap interferometric time-series analysis is used to derive mm/year interseismic velocities.
- The results indicate a decreasing locking depth of the southern Dead Sea fault towards the Red Sea rift.

Abstract

Interferometric Synthetic Aperture Radar (InSAR) data are increasingly being used to map interseismic deformation with ascending and descending-orbit observations allowing for resolving for the near-east and vertical displacement components. The north component has, however, been difficult to retrieve due to the limited sensitivity of standard InSAR observations in that direction. Here we address this problem by using time-series analysis of along-track interferometric observations in burst-overlap areas of the TOPS imaging mode of the Sentinel-1 radar satellites. We apply this method to the southern part of the near-north striking Dead Sea transform fault to show that the ~5 mm/year relative motion is well recovered. Furthermore, the results indicate the locking depth of the fault decreases towards the south as it enters the transtensional Gulf of Aqaba basin. Our results show that time-series analysis of burst-overlap interferometric observations can be used to obtain meaningful interseismic deformation rates of slow-moving and northerly-striking faults.

Plain Language Summary

Measurements of interseismic deformation near plate-boundary faults are used to estimate how large and how often major earthquakes are likely to occur and thus provide crucial input for regional seismic hazard assessments. Geodetic GPS data have primarily been used for this task, but increasingly Interferometric Synthetic Aperture Radar (InSAR) observations from satellites have provided useful information, particularly in areas where GPS observations are scarce. However, InSAR observations are only sensitive to the east and vertical components of deformation, but not to the north component, and are thus of limited use to study northerly striking earthquake faults. To address this problem, we combine advanced processing technique called burst-overlap interferometry (BOI) with time-series analysis of a large data set to retrieve millimeter per year details of north-south deformation. We apply this method to the north-striking southern Dead Sea fault to show that the earthquake hazard decreases towards the south as the fault enters Gulf of Aqaba and approaches the Red Sea rift. Our study demonstrates that this method of BOI time-series analysis allows mapping the interseismic deformation of slow-moving and north-striking faults.

1 Introduction

Geodetic measurements of interseismic deformation are used to estimate fault slip rates and locking depths and thus provide key information for seismic hazard assessments. While geodetic GNSS observations have been the main source of data for this purpose, InSAR has proven to be useful in many areas, especially where GNSS data are scarce, such as in eastern Anatolia (e.g., Wright et al. 2001; Walters et al. 2011; Cavalié and Jónsson, 2014; Hussain et al., 2018) and Tibet (e.g., Wright et al. 2004; Elliott et al., 2008; Cavalié et al., 2008). However, InSAR data from polar-orbiting radar satellites have limited sensitivity to the north component of displacement, meaning that standard InSAR observations are of little use for measuring interseismic deformation near north-south striking fault systems.

To retrieve full 3D surface displacements from SAR imaging, azimuth pixel-offset tracking is often used with both ascending and descending InSAR observations in cases when meter-scale displacements have occurred, such as in large earthquakes (e.g., Fialko et al. 2001, Jónsson et al., 2002; Wang and Jónsson, 2015; Akoglu et al., 2018). Similarly, azimuth split-beam interferometry, also known as multiple aperture interferometry (MAI), can be used to retrieve the

horizontal displacements parallel to the satellite track (Bechor and Zebker, 2006; Jung et al., 2012), which in many cases performs better than the azimuth pixel-offset tracking (e.g., Elliott et al., 2007; Wang and Jónsson, 2015; Jónsson 2012). Still, both azimuth pixel-tracking and MAI do not resolve mm- and cm-scale displacements well, and are therefore not suitable for mapping interseismic deformation.

The two Sentinel-1 satellites operate in the so-called TOPS (Terrain Observation with Progressive Scan) acquisition mode, in which the antenna beam is rotated forward during scanning bursts at a constant rate. Multiple bursts from three sub-swaths are then stitched together to form an image. In burst-overlap areas between neighboring bursts, the ground is imaged twice from two different view directions (forward-looking and backward-looking). The Sentinel-1 TOPS data thus provide an increased squint angle diversity within burst overlap areas, and hence achieve a better resolution of the along-track horizontal motion than conventional split-beam interferometry. This technique was first used to improve the coregistration between reference and secondary images (Scheiber and Moreira, 2000; Yague-Martinez et al., 2016). However, with burst-overlap interferometry (BOI) much better along-track displacements can be obtained, i.e., by making a double-difference interferogram for the pixels within the burst-overlap areas. The usefulness of BOI observations has already been demonstrated in earth science applications, e.g., in cases of co-seismic and post-seismic deformation (e.g., Grandin et al., 2016, Jiang et al., 2017, Yague-Martinez et al., 2019).

We here propose to use time-series analysis of a large number of along-track BOI observations to map interseismic surface deformation. We apply the method on the Dead Sea transform fault, which is a roughly north-south oriented left-lateral continental transform fault between the north-moving Arabian plate and the Sinai plate in the eastern Mediterranean region. The fault has produced many devastating earthquakes in the past and good mapping of the interseismic deformation is important for quantifying how rapid its stress loading is, providing inputs for seismic hazard assessments. The long-term slip rate estimates of the Dead Sea fault from offset geological and archaeological structures (e.g., Ginat et al., 1998; Klinger et al., 2000; Niemi et al., 2001) broadly agree with GPS results of the relative plate motion. These studies infer slip rates of the central and southern parts of the Dead Sea transform fault in the range of 3.8-6.0 mm/yr (e.g., McClusky et al., 2003; Wdowinski et al., 2004; Reilinger et al., 2006; Le Béon et al., 2008; Al-Tarazi et al., 2011; Sadeh et al., 2012; Masson et al., 2015; Saleh and Backer, 2015; Hamiel et al., 2018; Gomez et al., 2020). Estimates of the fault locking depth, however, range considerably and almost no information is available about the locking depth of the southernmost part of the Dead Sea fault in Gulf of Aqaba.

2 Methods

The double-difference interferograms of the BOI method are generated within the burst-overlap areas as follows:

$$\Phi_{\text{ovl}} = (r_1 \times s_1^*) \times (r_2 \times s_2^*)^*$$

where r and s represent the reference and secondary images, indices 1 and 2 the forward- and backward-looking views, and the * symbol denotes the conjugate of a complex number. We first geometrically align the reference and secondary images, use precise orbits (https://qc.sentinel1.eo.esa.int) for orbital and topographic corrections, and then multi-look the images by a factor of 20 in range and 4 in azimuth prior to the computation of the double-difference interferograms. In addition, an azimuth phase de-ramping is applied to remove the

azimuth phase ramp caused by Doppler Centroid variations (Yagüe-Martínez et al., 2016, Grandin, 2015). A spatial coherence mask with a threshold of 0.45 is then applied to discard unreliable phase values.

The key advantage of the double-difference BOI observations is that they are sensitive to horizontal ground motion in the along-track direction, as the common line-of-sight displacement component cancels out. The along-track displacement Δaz (in centimeters) is retrieved from the double-difference phase $\Delta\Phi_{\text{ovl}}$ (in radians) by:

$$\Delta az = \Delta\Phi_{\text{ovl}} \frac{\lambda}{4\pi\Delta\psi_{\text{ovl}}}$$

where $\Delta\psi_{\text{ovl}} = \Delta\eta_{\text{ovl}} k_{\psi}$ is the squint angle difference between two consecutive overlaps, with $\Delta\eta_{\text{ovl}}$ and k_{ψ} representing the time separation between overlaps and the antenna beam steering rate of the Sentinel-1 data, respectively (Grandin et al., 2016). For the standard Sentinel-1 interferometric wide swath (IW) TOPS imaging mode, the double difference phase is multiplied a factor ~21 cm/rad to obtain the along-track displacement (Grandin et al., 2016). Another advantage of the double-difference BOI observations is that the influence of the troposphere on the InSAR data is eliminated, but rapid spatial and temporal variations in the ionosphere can sometimes still induce artifacts in BOI observations.

To map horizontal along-track displacements near the Dead Sea transform fault, we use 161 and 143 of Sentinel-1 images acquired from both ascending and descending orbits, respectively. The images span the time period from October 2014 to September 2020. We then combine multiple BOI with SBAS (Small Baseline Subset) time-series analysis to retrieve the horizontal displacement history for each pixel in the burst-overlap areas. This procedure both enhances the performance of the surface displacement estimation and allows for removing most of the ionospheric effects.

3 Results

The derived along-track BOI velocities from both ascending and descending orbits show a clear and consistent velocity change across the Dead Sea fault from the western side to the eastern side of the fault (Fig. 1). The burst-overlap areas are about 1.5 km wide and 80 km long in each of the three sub-swaths of the Sentinel-1 IW imaging mode (here two sub-swaths were processed) and the distance between the burst-overlap areas is ~18 km. The burst overlap areas therefore spatially only cover ~10% of the ground and appear as narrow profiles in map view (Fig. 1). The derived along-track velocities are displayed with respect to the Sinai plate, i.e., the far-field velocities to the west are close to zero. We do this by averaging values at the far-western end of the profiles, within a 10 km∗60 km window covering multiple burst-overlap areas, and then subtract the average value from the result. The strike of the southern Dead Sea transform fault is about N10°E and the descending BOI observations thus almost exactly map the fault-parallel motion, with the results showing left-lateral ground displacement rate of ~5 mm/yr. The ascending along-track observations also indicate significant left-lateral motion, but of somewhat lesser magnitude, presumably due to the ~25° difference between the ascending-orbit track direction and the strike of the Dead Sea fault.

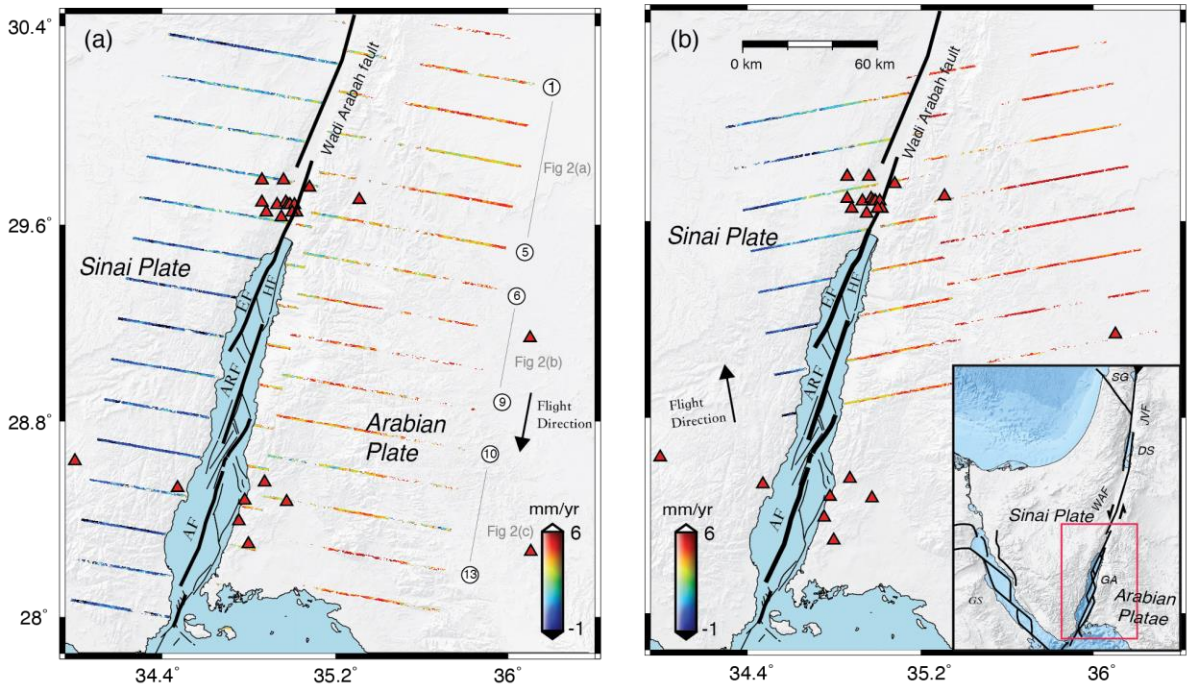

Figure 1. Map of the southern Dead Sea transform fault showing the derived Sentinel-1 burst-overlap interferometry (BOI) along-track (see arrow) interseismic velocities for (a) descending-orbit track T21 and (b) ascending track T87. The velocities are shown with respect to stable Sinai plate. Positive values represent ground movement towards the north, i.e., the descending along-track velocity is reversed to show the left-lateral motion. Red triangles show GNSS station locations (Hamiel et al., 2018 and Gomez et al., 2020), arrows the along-track satellite flying direction, and circled numbers the BOI profiles shown in Fig. 2. EF: Eilat Fault; HF: Haql Fault; ARF:Aragonese Fault; AF: Arnona fault. The inset shows the study area location. GA: Gulf of Aqaba; DS: Dead Sea; WAF: Wadi Arabah Fault; JVF, Jordan Valley Fault; SG, Sea of Galilee.

We first inspect the deformation across the Wadi Arabah fault section of the Dead Sea fault, north of Gulf of Aqaba. Here we select five burst-overlap areas across the fault, from 30.4°N in the north to 29.6°N in the south, and plot each profile with the median values and 1 sigma uncertainties. Each median value is obtained by including all the along-track BOI observations with the same fault-perpendicular distance (Fig. 2). While individual BOI velocity profiles show considerable scatter, the average of these profiles indicate a consistent and smooth velocity transition from the Sinai plate in the west to the Arabian plate in the east, clearly showing the left-lateral motion across the fault (Fig. 2a, bottom).

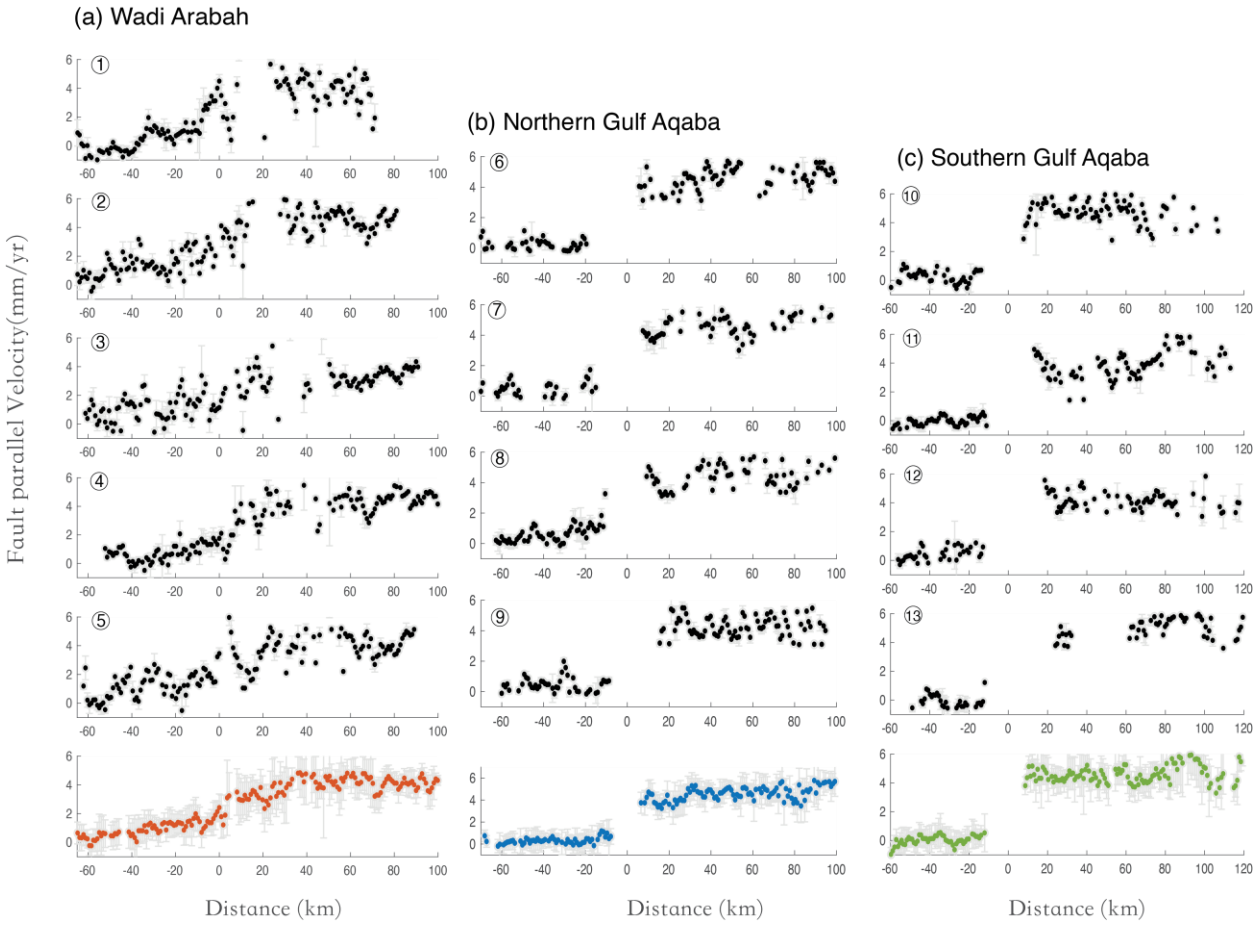

Figure 2. The fault-parallel BOI velocities across the Dead Sea fault along each burst-overlap area (from Fig. 1a) with median values plotted as black dots with 1 sigma uncertainties for the (a) Wadi Arabah fault, (b) northern Gulf of Aqaba, and (c) southern Gulf of Aqaba. The median value (black dot) is averaged with a 1.2km∗1.2km window and sampled with 1km spacing. The bottom rows show the stacked result from the profiles above.

Similarly, we use four burst-overlap profiles across the northern part of Gulf of Aqaba, stretching from 29.6°N in the north to 29°N near the southern end of Eilat fault, to assess the fault-parallel motion in this area. Here the left-lateral motion is also clearly visible, but more like a step function across the gap in the profile data, which corresponds to the gulf itself (Fig. 2b). In the southern gulf, four burst-overlap areas from 28.7°N to 28.2°N are shown and averaged indicating a similar sharp change across the gulf (Fig. 2c). The calculated stacked profile results for the three areas (bottom plots in Fig. 2) were derived by calculating the average of the individual burst-overlap profiles shown above, after eliminating outliers and locations with insufficient observations (i.e., less than 5 points). All the stacked profiles show clearly the ~5 mm/yr left-lateral motion but with notable differences in the profile shape across the fault.

4 Modeling

We use the stacked fault-parallel velocity profiles of the descending-orbit BOI results to estimate the locking depth of the southern Dead Sea fault based on the widely-used 1D screw dislocation model (Weertman and Weertman 1964; Savage and Burford 1973). In this model, fault parallel velocity (v_0) is a function of perpendicular distance to the fault (x):

$$v = v_0 + \frac{s}{\pi} tan^{-1}\left(\frac{x}{D}\right)$$

where v_0 defines a static offset, s and D are the long-term slip rate and locking depth, respectively. A grid-search method was applied to search for the best slip rate and locking depth values over ranges of 0-8 mm/yr and 0–30 km with 0.1 mm/yr and 0.5 km intervals. The modeling solved for three parameters: slip rate s, locking depth D, and the offset v_0. The RMS (root mean square) misfit between the model prediction and observations for each combination of the parameters was calculated to find the optimal values of the slip rate and locking depth. The uncertainties of the obtained model parameters were then estimated by first perturbing the dataset with Gaussian noise and then searching for the optimal parameters of 1000 perturbed datasets, yielding a robust estimation of the model parameter uncertainties.

We separately estimate the locking depth for three different sections of the southern Dead Sea fault, i.e., for the Wadi Arabah fault in the north, and then the northern and southern Gulf of Aqaba. For each fault section, we use the average BOI time-series velocities from several burst-overlap areas (Fig. 2, bottom). For the Wadi Arabah fault, the smooth velocity transition from Sinai to Arabia yields a relative deep locking depth of 18.9±6.4 km with a slip rate of 4.7±0.45 mm/yr (Fig. 3). The fault-parallel BOI velocities in this area and the derived model parameters are in good agreement with published GPS results (Hamiel et al., 2018). When these GPS velocities from both near- and far-field campaign stations across the fault are used alone, they yield a similar locking depth of 19.9±7.7 km and a slip rate of 5.0±0.8 mm/yr (Fig. 3a), consistent with our BOI result.

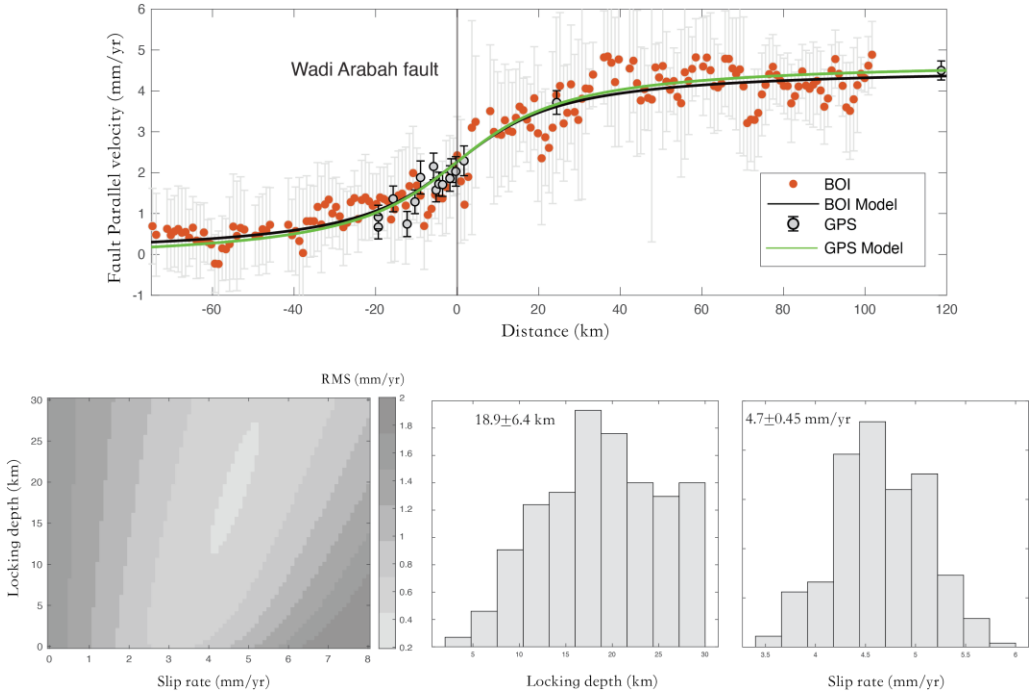

Figure 3. Observed fault-parallel BOI velocities (red dots) across the Wadi Arabah fault with 1σ uncertainties (from Fig. 2a) in comparison with the screw-dislocation model prediction. Gray dots show fault-parallel GPS velocities with 1σ uncertainties (Hamiel et al., 2018), shifted to match the BOI velocity reference, and the model prediction using the GPS data alone (green line). The misfit (bottom left) shows the trade-off between estimated locking depth and slip rate and the histograms indicate the model parameter uncertainties assessed from the Monte Carlo simulation.

For the Gulf of Aqaba, we assume a single vertical fault extending from the southernmost tip of Arnona fault in the south to the northernmost tip of the gulf with a strike of 16°. We estimate a mean slip rate of 5.0±0.4 mm/year with a locking depth of 7.7±3.6 km for northern part of the gulf (Fig. 4), i.e., significantly shallower locking depth than for Wadi Arabah. This indicates that the moment accumulation rate of the fault decreases significantly as it enters the transtensional Gulf of Aqaba basin. The estimated locking depth of the southern Gulf of Aqaba is even shallower, or only 3.9±2.9 km with a slip rate of 4.9±0.33 mm/yr (Fig. 5). This means that we cannot exclude (at 2σ) the possibility that the fault is creeping at this location. Using the limited GPS results that have been published in the gulf area, and discarding far-field sites with large variations, we also obtain a very shallow locking depth of 1.5 km for the southern part of the gulf and a slip rate of 5.2 mm/yr. Combined, the BOI and GPS results yield a locking depth of 3.5 km and a slip rate of 4.9 mm/yr (Fig. 5). Overall, the results suggest that the locking depth of the southern Dead Sea fault gradually decreases as the fault extends into the Gulf of Aqaba and towards the active Red Sea rift zone.

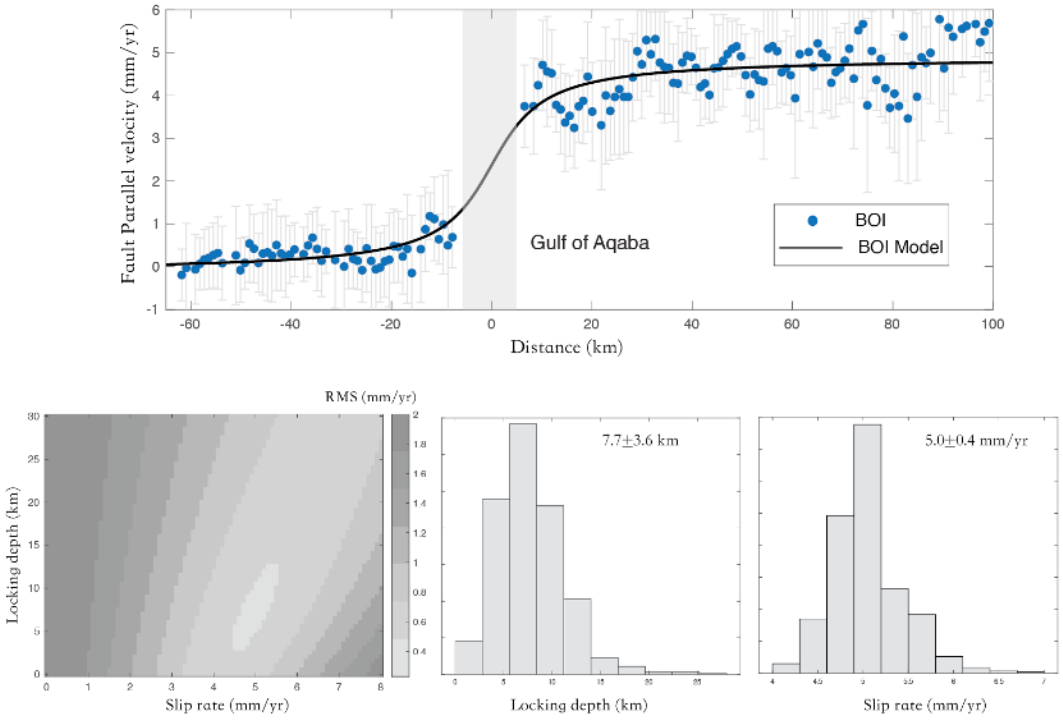

Figure 4. Fault-parallel BOI velocities (blue dots) with 1σ uncertainties across the northern Gulf of Aqaba (from Fig. 2b) in comparison with the best screw-dislocation model prediction. The lower panels are as in Fig. 3.

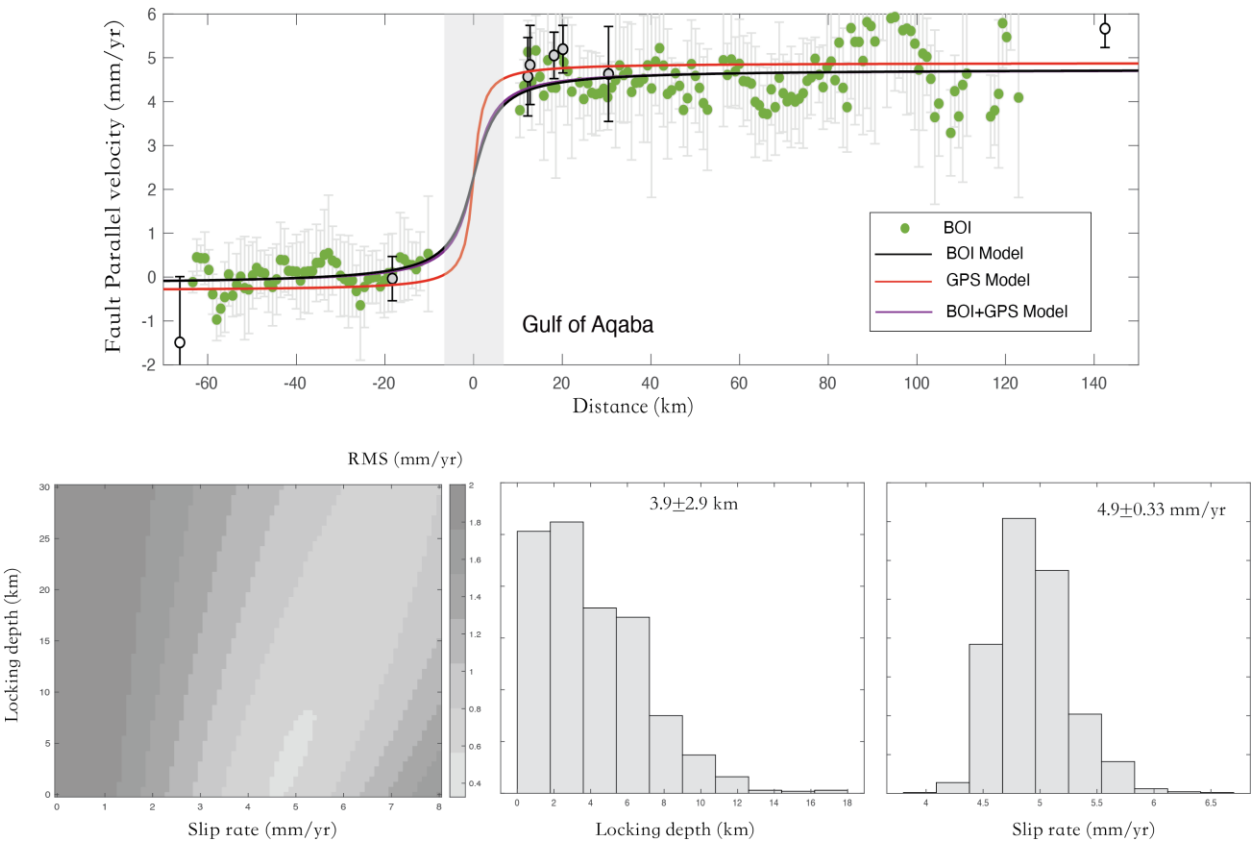

Figure 5. Fault-parallel BOI velocities (green dots) with 1σ uncertainties across the southern Gulf of Aqaba (from Fig. 2c) in comparison with GPS and model predictions (see text). Gray dots represent GPS observations with 1σ uncertainty (Gomez et al., 2020), while white GPS dots were dismissed from the analysis. The lower panels are as in Fig. 3.

5 Discussion and Conclusions

Our BOI results show a clear left-lateral movement focused on the southern Dead Sea fault of 4.5-5 mm/yr, which is in agreement with both geologic and GPS estimates of the fault slip rate (e.g., Bartov et al., 1980; Le Béon et al., 2008; Hamiel et al., 2018; Gomez et al., 2020). The BOI velocities are not calibrated in any way by GPS data or other land-based measurements, i.e., they are derived solely from the Sentinel-1 BOI time-series analysis, and thus provide a new independent estimate of the slip rate of the southern Dead Sea fault. In addition, not only is the relative plate motion well recovered, details of the interseismic deformation near the fault are also resolved to less than 1 mm/yr (e.g., Fig. 3). This demonstrates, for the first time, that accurate interseismic velocities can be derived for slow-moving north-striking faults using Sentinel-1 BOI data alone when a large number of BOI observations is used.

Previous studies of the locking depth of the southern Dead Sea fault mostly focused on the segment north of the Gulf of Aqaba, due to lack of GPS sites near the gulf. Similar as with the slip rate results, our locking depth estimate north of the gulf in Wadi Arabah agrees well with published GPS results (e.g., Hamiel et al., 2018). Further south, we have limited GPS data to compare with. However, despite the lack of near-field data due to the offshore location of the fault in the gulf, the BOI results clearly indicate a sharper transition of the relative motion across the fault than in Wadi Arabah (Fig. 2). Our results thus suggest a decreasing locking depth from

the north into the gulf and towards the Red Sea rift. The estimated locking depths are much lower than in Wadi Arabah, or 7.7±3.6 km in the northern gulf and only 3.9±2.9 km in the southern gulf, meaning that we cannot exclude continuous creep (at 2 σ) of the Arnona fault in the south. The structure of the Gulf of Aqaba shows that it has experienced significant extension as well as left-lateral slip. The active extension and normal faulting are evident by the stark topographic contrast between the 900-1800 m deep gulf basins and the surrounding ~2000 m high mountains. The gulf has thus been subject to significant crustal thinning and probably has elevated heat flow that might explain the smaller locking depth. The decreasing locking depth towards the south may also imply an increasing influence from the Red Sea rift, located just south of the gulf. Whatever the explanation for the smaller locking depth is, the result indicates a lower moment accumulation rate on this portion of the fault system and thus lower earthquake hazard as compared to the fault north of the gulf.

Using six years of Sentinel-1 data from Oct. 2014 to Sep. 2020, our analysis and uncertainty assessment assumes a constant deformation rate during the study period. If our BOI uncertainties are underestimated, the level of confidence of the estimated model parameters could be too optimistic (e.g., Duputel et al., 2014). However, the BOI uncertainties seem rather to be overestimated, judging from the consistency with GPS (Fig. 3) and the smooth gradual velocity changes along each derived velocity profile (Fig. 2, bottom), implying that our data errors and model confidence levels are on the conservative side. Therefore, the limitations of the simple 1D screw-dislocation model as well as the uncertainty of the exact fault location on the seafloor within the gulf are probably more important. Fault mapping within the gulf has revealed en-echelon fault patterns with over-lapping faults and pull-apart basins that are far from a single straight fault strand in the middle of the gulf. In the northern gulf, for example, the Eilat and Haql faults bound the Eilat basin on the western and eastern side, respectively, with each fault near the opposing gulf coastlines (Ribot et al., 2020). The BOI results show more interseismic deformation on the western coast (Fig. 4), indicating the deformation is rather focused on the Eilat fault than the Haql fault. However, whichever the main active fault is, the deformation in the gulf is much more focused than to the north in Wadi Arabah, signifying a smaller locking depth.

We have demonstrated the applicability of BOI time-series analysis to map interseismic deformation across slow-moving north-striking faults, like the southern Dead Sea fault. Without external constraints, the BOI time-series results reveal a fault-parallel velocity of 4.5-5 mm/yr, consistent with GPS observations, as well as details of the near-fault interseismic deformation pattern. The results furthermore indicate that the fault locking depth decreases towards the south as the fault enters Gulf of Aqaba and becomes closer to the Red Sea rift. The achievable ground velocity accuracy depends on temporal coherence and the number of images used in the BOI time-series analysis, and can become lower than 1 millimeter per year when more than hundred images are combined.

Acknowledgments

This study was supported by King Abdullah University of Science and Technology (KAUST), awards BAS/1/1353-01-01 and OSR-CRG2020-4335. This study was supported by King Abdullah University of Science and Technology (KAUST), awards BAS/1/1353-01-01 and OSR-CRG2020-4335. Sentinel-1 SAR images can be freely accessed from the Copernicus Open Access Hub (https://scihub.copernicus.eu). Sentinel-1 interferograms are processed with

software GAMMA (Werner et al., 2001). GPS data is available through Hamiel et al. 2018 and Gomez et al., 2020. Figures are prepared using Generic Mapping Tools (Wessel et al., 2013) and MATLAB.

References

Akoglu, H. (2018). User's guide to correlation coefficients. *Turkish journal of emergency medicine*, 18(3), 91-93.

Al Tarazi, E., Abu Rajab, J., Gomez, F., Cochran, W., Jaafar, R., & Ferry, M. (2011). GPS measurements of near - field deformation along the southern Dead Sea Fault System. *Geochemistry, Geophysics, Geosystems*, 12(12).

Bartov, Y., Steinitz, G., Eyal, M., & Eyal, Y. (1980). Sinistral movement along the Gulf of Aqaba—its age and relation to the opening of the Red Sea. *Nature*, 285(5762), 220-222.

Bechor, N. B., & Zebker, H. A. (2006). Measuring two-dimensional movements using a single InSAR pair. *Geophysical research letters*, 33(16).

Cavalié, O., & Jónsson, S. (2014). Block - like plate movements in eastern Anatolia observed by InSAR. *Geophysical Research Letters*, 41(1), 26-31.

Cavalié, O., Lasserre, C., Doin, M. P., Peltzer, G., Sun, J., Xu, X., et al. (2008). Measurement of interseismic strain across the Haiyuan fault (Gansu, China), by InSAR. *Earth and Planetary Science Letters*, 275(3-4), 246-257.

Duputel, Z., Agram, P. S., Simons, M., Minson, S. E., & Beck, J. L. (2014). Accounting for prediction uncertainty when inferring subsurface fault slip. *Geophysical journal international*, 197(1), 464-482.

Elliott, J. L., Freymueller, J. T., & Rabus, B. (2007). Coseismic deformation of the 2002 Denali fault earthquake: Contributions from synthetic aperture radar range offsets. *Journal of Geophysical Research: Solid Earth*, 112(B6).

Elliott, J. R., Biggs, J., Parsons, B., & Wright, T. J. (2008). InSAR slip rate determination on the Altyn Tagh Fault, northern Tibet, in the presence of topographically correlated atmospheric delays. *Geophysical Research Letters*, 35(12).

Fialko, Y., Simons, M., & Agnew, D. (2001). The complete (3-D) surface displacement field in the epicentral area of the 1999 Mw7. 1 Hector Mine earthquake, California, from space geodetic observations. *Geophysical research letters*, 28(16), 3063-3066.

Ginat, H., Enzel, Y., & Avni, Y. (1998). Translocated Plio-Pleistocene drainage systems along the Arava fault of the Dead Sea transform. *Tectonophysics*, 284(1-2), 151-160.

Gomez, F., Cochran, W. J., Yassminh, R., Jaafar, R., Reilinger, R., Floyd, M., et al. (2020). Fragmentation of the Sinai Plate indicated by spatial variation in present-day slip rate along the Dead Sea Fault System. *Geophysical Journal International*, 221(3), 1913-1940.

Grandin, R. (2015). Interferometric processing of SLC Sentinel-1 TOPS data. In FRINGE'15: Advances in the Science and Applications of SAR Interferometry and Sentinel-1 InSAR Workshop, Frascati, Italy.

345 Grandin, R., Klein, E., Métois, M., & Vigny, C. (2016). Three-dimensional displacement field of
346 the 2015 Mw8. 3 Illapel earthquake (Chile) from across-and along-track Sentinel-1 TOPS
347 interferometry. *Geophysical Research Letters*, 43(6), 2552-2561.

348 Hamiel, Y., Masson, F., Piatibratova, O., & Mizrahi, Y. (2018). GPS measurements of crustal
349 deformation across the southern Arava Valley section of the Dead Sea Fault and implications to
350 regional seismic hazard assessment. *Tectonophysics*, 724, 171-178.

351 Hussain, Z., Arslan, M., Malik, M. H., Mohsin, M., Iqbal, S., & Afzal, M. (2018). Integrated
352 perspectives on the use of bacterial endophytes in horizontal flow constructed wetlands for the
353 treatment of liquid textile effluent: phytoremediation advances in the field. *Journal of*
354 *environmental management*, 224, 387-395.

355 Jiang, H., Feng, G., Wang, T., & Bürgmann, R. (2017). Toward full exploitation of coherent and
356 incoherent information in Sentinel - 1 TOPS data for retrieving surface displacement:
357 Application to the 2016 Kumamoto (Japan) earthquake. *Geophysical Research Letters*, 44(4),
358 1758-1767.

359 Jónsson, S. (2012). Tensile rock mass strength estimated using InSAR. *Geophysical research*
360 *letters*, 39(21).

361 Jónsson, S., Zebker, H., Segall, P., & Amelung, F. (2002). Fault slip distribution of the 1999 M
362 w 7.1 Hector Mine, California, earthquake, estimated from satellite radar and GPS measurements.
363 *Bulletin of the Seismological Society of America*, 92(4), 1377-1389.

364 Jung, H. S., Lu, Z., & Zhang, L. (2012). Feasibility of along-track displacement measurement
365 from Sentinel-1 interferometric wide-swath mode. *IEEE Transactions on Geoscience and*
366 *Remote Sensing*, 51(1), 573-578.

367 Klinger, Y., Avouac, J. P., Dorbath, L., Karaki, N. A., & Tisnerat, N. (2000). Seismic behaviour
368 of the Dead Sea fault along Araba valley, Jordan. *Geophysical Journal International*, 142(3),
369 769-782.

370 Le Béon, M., Klinger, Y., Amrat, A. Q., Agnon, A., Dorbath, L., Baer, G., et al. (2008). Slip rate
371 and locking depth from GPS profiles across the southern Dead Sea Transform. *Journal of*
372 *Geophysical Research: Solid Earth*, 113(B11).

373 Masson, F., Hamiel, Y., Agnon, A., Klinger, Y., & Deprez, A. (2015). Variable behavior of the
374 Dead Sea Fault along the southern Arava segment from GPS measurements. *comptes rendus*
375 *geoscience*, 347(4), 161-169.

376 McClusky, S., Reilinger, R., Mahmoud, S., Ben Sari, D., & Tealeb, A. (2003). GPS constraints
377 on Africa (Nubia) and Arabia plate motions. *Geophysical Journal International*, 155(1), 126-138.

378 Niemi, T. M., Zhang, H., Atallah, M., & Harrison, J. B. J. (2001). Late Pleistocene and Holocene
379 slip rate of the northern Wadi Araba fault, Dead Sea transform, Jordan. *Journal of seismology*,
380 5(3), 449-474.

381 Reilinger, R., McClusky, S., Vernant, P., Lawrence, S., Ergintav, S., Cakmak, R., et al. (2006).
382 GPS constraints on continental deformation in the Africa - Arabia - Eurasia continental collision
383 zone and implications for the dynamics of plate interactions. *Journal of Geophysical Research:*
384 *Solid Earth*, 111(B5).

Ribot, M., Klinger, Y., Jónsson, S., Avsar, U., Pons-Branchu, E., Matrau, R., et al. (2020). Active faults' geometry in the Gulf of Aqaba, southern Dead Sea fault, illuminated by multi beam bathymetric data.

Sadeh, M., Hamiel, Y., Ziv, A., Bock, Y., Fang, P., & Wdowinski, S. (2012). Crustal deformation along the Dead Sea transform and the Carmel Fault inferred from 12 years of GPS measurements. *Journal of Geophysical Research: Solid Earth*, 117(B8).

Saleh, M., & Becker, M. (2015). New constraints on the Nubia–Sinai–Dead Sea fault crustal motion. *Tectonophysics*, 651, 79-98.

Savage, J. C., & Burford, R. O. (1973). Geodetic determination of relative plate motion in central California. *Journal of Geophysical Research*, 78(5), 832-845.

Scheiber, R., & Moreira, A. (2000). Coregistration of interferometric SAR images using spectral diversity. *IEEE Transactions on Geoscience and Remote Sensing*, 38(5), 2179-2191.

Walters, R. J., Holley, R. J., Parsons, B., & Wright, T. J. (2011). Interseismic strain accumulation across the North Anatolian Fault from Envisat InSAR measurements. *Geophysical research letters*, 38(5).

Wang, T., & Jónsson, S. (2015). Improved SAR amplitude image offset measurements for deriving three-dimensional coseismic displacements. *IEEE Journal of Selected Topics in Applied Earth Observations and Remote Sensing*, 8(7), 3271-3278.

Wdowinski, S., Bock, Y., Baer, G., Prawirodirdjo, L., Bechor, N., Naaman, S., et al. (2004). GPS measurements of current crustal movements along the Dead Sea Fault. *Journal of Geophysical Research: Solid Earth*, 109(B5).

Weertman, J., & Weertman, J. R. (1964). Elementary dislocation theory. Macmillan.

Werner, C., Wegmüller, U., Strozzi, T., & Wiesmann, A. (2000). Gamma SAR and interferometric processing software. *In Proceedings of the ers-envisat symposium*, Gothenburg, Sweden (Vol. 1620, p. 1620).

Wessel, P., Smith, W. H., Scharroo, R., Luis, J., & Wobbe, F. (2013). Generic mapping tools: improved version released. Eos, *Transactions American Geophysical Union*, 94(45), 409-410.

Wright, T. J., Parsons, B. E., & Lu, Z. (2004). Toward mapping surface deformation in three dimensions using InSAR. *Geophysical Research Letters*, 31(1).

Wright, T., Parsons, B., & Fielding, E. (2001). Measurement of interseismic strain accumulation across the North Anatolian Fault by satellite radar interferometry. *Geophysical Research Letters*, 28(10), 2117-2120.

Yagüe-Martínez, N., Prats-Iraola, P., Gonzalez, F. R., Brcic, R., Shau, R., Geudtner, D., et al. (2016). Interferometric processing of Sentinel-1 TOPS data. *IEEE Transactions on Geoscience and Remote Sensing*, 54(4), 2220-2234.

Yagüe-Martínez, N., Prats-Iraola, P., Pinheiro, M., & Jaeger, M. (2019). Exploitation of burst overlapping areas of tops data. Application to sentinel-1. *In IGARSS 2019-2019 IEEE International Geoscience and Remote Sensing Symposium* (pp. 2066-2069). IEEE.